

# Mesostructures of Cobalt Nanocrystals. 1. Experiment and Theory

V. Germain, J. Richardi, D. Inger, and M. P. Pileni\*

Laboratoire des Matériaux Mesoscopiques et Nanométriques U.M.R. 7070, Université Pierre et Marie Curie, BP 52, 4 place Jussieu, 75005 Paris, France

Received: September 23, 2004; In Final Form: December 8, 2004

Solid mesostructures made of cylinders are produced by the slow evaporation of cobalt nanocrystals dispersed in hexane and subjected to an applied field perpendicular to the substrate. Varying the initial nanocrystal concentration is found to be an efficient method for changing the pattern size. The experimental structures and the theoretical predictions based on the minimization of the total free energy are in good agreement. A comparison of experiment with theory allowed us to conclude that the mesostructures form as a result of a liquid–gas phase transition during the evaporation process. Within the theoretical model and the experimental data, it is concluded that the phase ratio of the magnetic to the total volume and the height of the cylinders govern the pattern geometry. In contrast, because of the saturation of the magnetization curve, the mesostructures are not influenced by the field strength.

## 1. Introduction

Solid mesostructures made of cobalt nanocrystals were recently discovered by the evaporation of solutions of magnetic nanoparticles in a high magnetic field.<sup>1</sup> Labyrinthine patterns and hexagonal arrays of cylinders of submicron dimensions were obtained. Similar structures were previously observed in other ferrofluid systems,<sup>2–6</sup> where they were explained by an interplay of interfacial and magnetic forces.<sup>3,7–9</sup> In contrast to this, the new mesostructures of cobalt nanocrystals are solid. However, it can be assumed that the patterns are formed in the liquid film during the solvent evaporation. It is remarkable that the mesostructures are able to survive the complete solvent evaporation, even when they are often markedly damaged.<sup>10</sup> This opens a new way to fabricate artificial, tailored structures at submicron scales, which are of interest both for fundamental research and for technological applications. An attractive feature of this bottom-up technique is that it does not require very pure facilities as other methods such as nanolithography do.<sup>11</sup>

Here, the mechanism of structure formation is investigated. In particular, we discuss the nature of the interface, which separates the mesostructures from their surroundings during the pattern formation. Then, we present the various parameters involved in the control of the characteristic sizes of the cylinders constituting the patterns. Our approach is both experimental and theoretical. Experimentally, the influences of magnetic field strength and nanocrystal concentration on the mesostructures are investigated. In particular, the variation in particle concentration turns out to be an efficient method to change the pattern size. Then, the experimental data are interpreted using a recently developed nonlinear theory of ferrofluid pattern formation.<sup>12</sup> In this study, we will focus on hexagonal structures because their geometry can be more accurately measured than those of labyrinths.

## 2. Method

**2-1. Synthesis of Cobalt Nanocrystals.** Cobalt nanocrystals are synthesized by using reverse micelles of  $5 \times 10^{-2} \text{ mol L}^{-1}$

$\text{Co(AOT)}_2/\text{water/isooctane}$ , as described elsewhere.<sup>13,14</sup> The amount of water, defined as  $w = [\text{H}_2\text{O}]/[\text{Co(AOT)}_2]$ , is kept at 32.  $\text{Co(AOT)}_2$  is reduced by the addition of sodium borohydride ( $[\text{NaBH}_4] = 3 \times 10^{-1} \text{ mol L}^{-1}$ ). The cobalt nanocrystals are coated by adding 0.2 M lauric acid ( $\text{C}_{12}\text{H}_{26}\text{O}_2$ ) to the solution; then, ethanol is added and the solution centrifuged. A black precipitate containing the nanocrystals is obtained. This procedure is repeated several times to purify the nanocrystals. The solution containing nanocrystals dispersed in hexane is centrifuged, and the supernatant containing the smallest nanocrystals is collected. This leads to the synthesis of cobalt nanocrystals with an average diameter of 7.2 nm and a size distribution of 13%. Because the formation of mesoscopic structures needs a large amount of nanocrystals, the procedure described above is repeated several times and the samples are mixed together. This last procedure induces a slight increase in the size distribution of the nanocrystals (20%), keeping the same average size. Cobalt acetate, lauric acid, and sodium borohydride were from Aldrich, isooctane and hexane were from Fluka, and di(ethylhexyl)sulfosuccinate was from Sigma. All of the chemicals were used without further purification.

To determine the influence of cobalt nanocrystal concentration on the mesostructure morphology, three concentrations of cobalt atoms ( $0.24 \times 10^{-3}$ ,  $0.48 \times 10^{-3}$ , and  $9.5 \times 10^{-3} \text{ mol L}^{-1}$ ) are chosen, that is, particle concentrations of  $9.7 \times 10^{-9}$ ,  $1.9 \times 10^{-8}$ , and  $3.9 \times 10^{-7} \text{ mol L}^{-1}$ .

**2-2. Fabrication of Mesoscopic Structures of Cobalt Nanocrystals.** To form the mesostructures, 200  $\mu\text{L}$  of cobalt nanocrystals dispersed in hexane is deposited in a beaker containing a freshly cleaved  $5 \times 5 \text{ mm}$  highly oriented pyrolytic graphite substrate. To increase the evaporation time, the beaker is covered by Parafilm. It is then placed between the coils of an electromagnet with a magnetic field applied perpendicular to the substrate. The magnetic field with various strengths (0.17, 0.33, 0.46, and 0.59 T) is applied during the evaporation and gives rise to solid mesostructures, stable even after switching off the magnetic field. After complete solvent evaporation, the substrate is carefully removed from the beaker and imaged with a scanning electron microscope (SEM).<sup>15</sup>

\* To whom correspondence should be addressed. E-mail: pileni@sri.jussieu.fr.

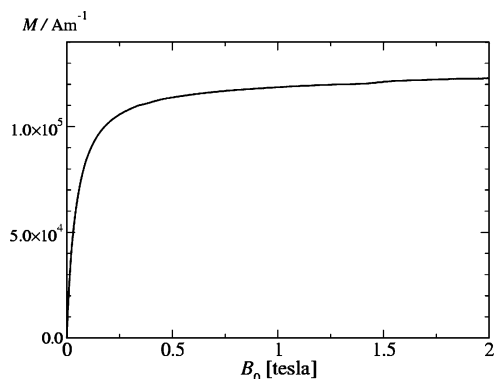


**Figure 1.** Experimental magnetization curve of a deposition of cobalt nanocrystals obtained by SQUID.

**2-3. Theory.** A theory is developed that yields the radius  $r_0$  of cylinders forming a hexagonal pattern as a function of the external field  $H_0$ , the ratio of the magnetic phase to the total volume  $\Phi$ , and the cylinder height  $L$ . It is assumed that the pattern formation is determined by a minimization of the total free energy. Thus, any influence of the dynamics of pattern formation on the geometry of the final structures is neglected. The hexagonal structures are idealized as a hexagonal array of cylinders made of cobalt nanocrystals. For a given set of  $H_0$ ,  $\Phi$ , and  $L$ , the radius  $r_0$  is obtained by minimization of the free energy ( $f_h$ ) per surface area:<sup>3,8,12</sup>

$$f_h = \Phi \frac{2L}{r_0} \sigma + \frac{F_m}{s_h} \quad (1)$$

where  $s_h$  is the surface area per cylinder. The first term represents the surface energy, which is characterized by the interfacial tension  $\sigma$  between the magnetic cylinders and their environment. Because this interfacial tension is usually determined by short-range, nondipolar forces, we can assume that it does not depend on the external field.<sup>16</sup> The proposed energy function does not contain an entropy term. A correct description of the entropy in this kind of system is still an open issue.<sup>8,12,17</sup> Using the entropy term proposed in ref 12, we found that the entropy for heights above 1  $\mu\text{m}$  does not significantly influence the structure. Because all of the experimentally observed structures except one have heights greater than 1  $\mu\text{m}$ , the entropy is neglected. The second term on the right side of eq 1 represents the magnetic energy given by

$$F_m = \int d\vec{r} \int_0^{B^-} \vec{H}' d\vec{B}' - \frac{\mu_0}{2} \int d\vec{r} H_0^2 \quad (2)$$

Primes are used for  $H$  and  $B$  to make a difference with the integration limit. The magnetic induction at a point  $\vec{r}$  in the hexagonal structure is calculated from the magnetization  $\vec{M}(\vec{r})$  and the total magnetic field  $\vec{H}(\vec{r})$ :

$$\vec{B}(\vec{r}) = \mu_0 [\vec{H}(\vec{r}) + \vec{M}(\vec{r})] \quad (3)$$

The magnetization is a nonlinear function of the total magnetic field.

$$M = f(H) \quad (4)$$

For our calculations, an experimental magnetization curve of a deposition of cobalt nanocrystals is used. It was measured using a superconducting quantum interference device (SQUID) and is shown in Figure 1. The measured total magnetization of the sample is divided by the volume occupied by the nanocrystal

film. An estimate of this volume is obtained from the mass  $m_d$  of the deposited nanocrystals using the equation

$$V_d = \frac{1}{0.638 m_d \rho_{\text{Co}}} \left( \frac{d_c}{d_p} \right)^3 \quad (5)$$

$\rho_{\text{Co}}$  is the mass density of cobalt ( $8.84 \times 10^3 \text{ kg m}^{-3}$ ).  $d_p$  and  $d_c$  are the particle diameter (7.2 nm) and the center-to-center distance (10.46 nm) of the cobalt nanocrystals, respectively. Both values are taken from the literature.<sup>18</sup> Moreover, we assume that the volume fraction of the nanocrystals is close to the packing fraction of randomly packed spheres (0.638).

The total field  $\vec{H}(\vec{r})$  within the hexagonal structure is reduced with respect to the external field  $\vec{H}_0$  because of the negative demagnetization field  $\vec{H}_d(\vec{r})$ :

$$\vec{H}(\vec{r}) = \vec{H}_0 + \vec{H}_d(\vec{r}) \quad (6)$$

The demagnetization field is caused by the magnetization of the cobalt nanocrystals. The calculation of  $\vec{H}_d(\vec{r})$  is explained elsewhere.<sup>19,20</sup> The structures observed experimentally usually extend over a wide area of the substrate. For the sake of calculations, the structures are assumed to be infinite in the direction parallel to the substrate. The correct treatment of the long-range dipolar interactions in this case is derived in ref 19. An exact calculation of the demagnetization field is, even on modern computers, too time consuming. Therefore, a volume-averaged magnetization is used during the evaluation of  $\vec{H}_d(\vec{r})$ .<sup>20</sup> We have recently shown that the theoretical results are not affected by this approach, in contrast to other approximations.<sup>12,20</sup> For a given set of  $H_0$ ,  $\Phi$ ,  $L$ , and  $r_0$ , the magnetization is obtained by an iterative procedure, which starts from an arbitrary initial magnetization. Then, at a large number of points in the cylinder, the demagnetization field is calculated from the initial magnetization. A new estimate of  $\vec{M}(\vec{r})$  is calculated from the magnetization curve. Because the function  $M = f(H)$ , shown in Figure 1, is tabulated on a grid of  $H$  values, the magnetization for intermediate field strengths is calculated by interpolation. A new demagnetization field is calculated from the new magnetization. This procedure is iterated until the magnetization evaluated from the field agrees with that used to compute the demagnetization field. The nonlinear relationship between  $M$  and  $H$  markedly complicates the calculation of the magnetic energy.<sup>12</sup> To obtain numerically stable magnetic energies, eq 2 must be recast into the form

$$F_m = \int_{V_m} \int_0^{B^-} \vec{H}' d\vec{B}' d\vec{r} - \mu_0 \vec{H}_0 \int_{V_m} \vec{M} d\vec{r} - \mu_0 \vec{H}_0 \int_{V_m} \vec{H}_d d\vec{r} - \frac{\mu_0}{2} \int_{V_m} \vec{H}_d \vec{M} d\vec{r} - \frac{\mu_0}{2} \int_{V_m} \vec{H}_d^2 d\vec{r} \quad (7)$$

In contrast to eq 2, the integrals of the new expression are limited to the volume  $V_m$  of the magnetic phase. Therefore, the size of the spatial grid used for the numerical integration can be largely reduced, which yields a large gain in computing time. Moreover, the magnetic energy calculated from eq 7 rapidly converges when a finer grid for integration is used, which is not the case for eq 6. Note that the magnetic energies  $F_m$  are calculated on a grid of values of  $H_0$ ,  $r_0$ , and  $\Phi$  and are stored. Because the energy depends linearly on the height,  $F_m$  is determined at only one height. During the determination of  $r_0$  by energy minimization, the magnetic energies are calculated by interpolation from the tabulated  $F_m$  values. All calculations were carried out using the homemade FORTRAN package HEXALAB.<sup>21</sup>



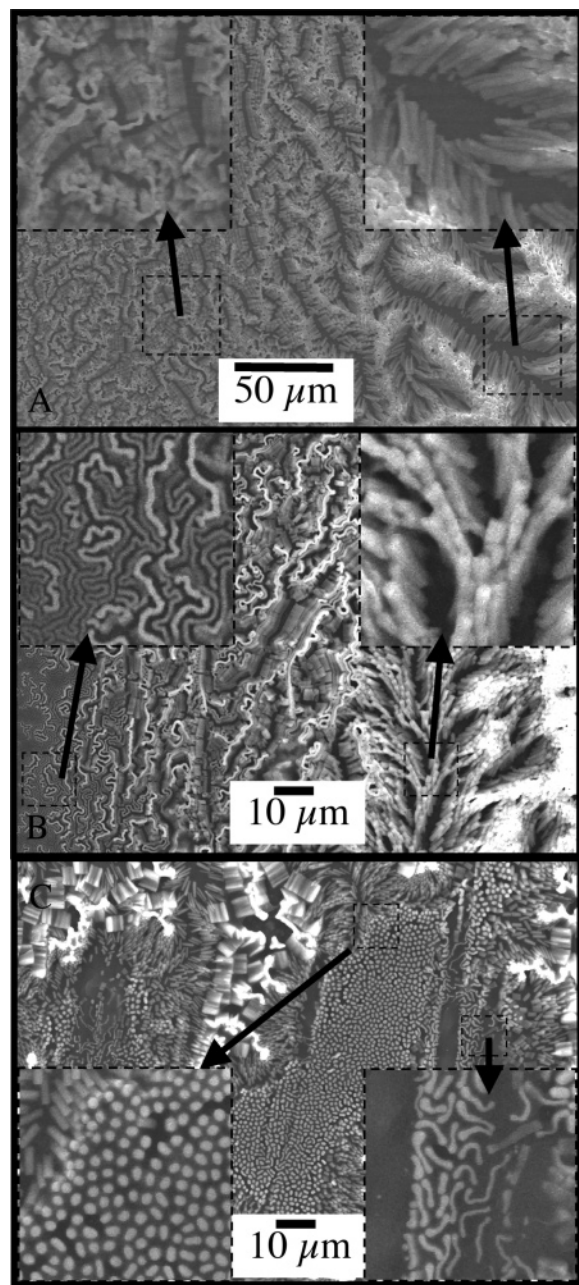


**Figure 2.** SEM images of a substrate showing the coexistence of the cobalt labyrinthine and cylinder patterns: (A) magnetic field 0.33 T, solution concentration  $9.53 \times 10^{-3} \text{ mol L}^{-1}$ ; (B) magnetic field 0.46 T, solution concentration  $4.76 \times 10^{-4} \text{ mol L}^{-1}$ ; (C) magnetic field 0.59 T, solution concentration  $2.38 \times 10^{-4} \text{ mol L}^{-1}$ . The insets for A–C are magnifications of the two structures.

### 3. Results and Discussions

**3-1. Characterization of the Cobalt Nanocrystal Mesostructures.** Figure 2 shows the SEM patterns obtained at various strengths of applied field and various nanocrystal initial concentrations used before the evaporation process. Labyrinthine and hexagonal mesostructures coexist whatever the applied magnetic field strength and the cobalt nanocrystal concentration are. These structures are similar to those obtained with ferrofluids in Hele-Shaw cells.<sup>2–6,22</sup> However, in contrast, the hexagonal structures are most often collapsed (Figure 2). This is in agreement with patterns obtained recently with cobalt nanoparticles.<sup>23</sup> Figure 2C shows upright cylinders. From the patterns shown in Figure 2, it is deduced that the strength of the applied magnetic field does not form one preferential

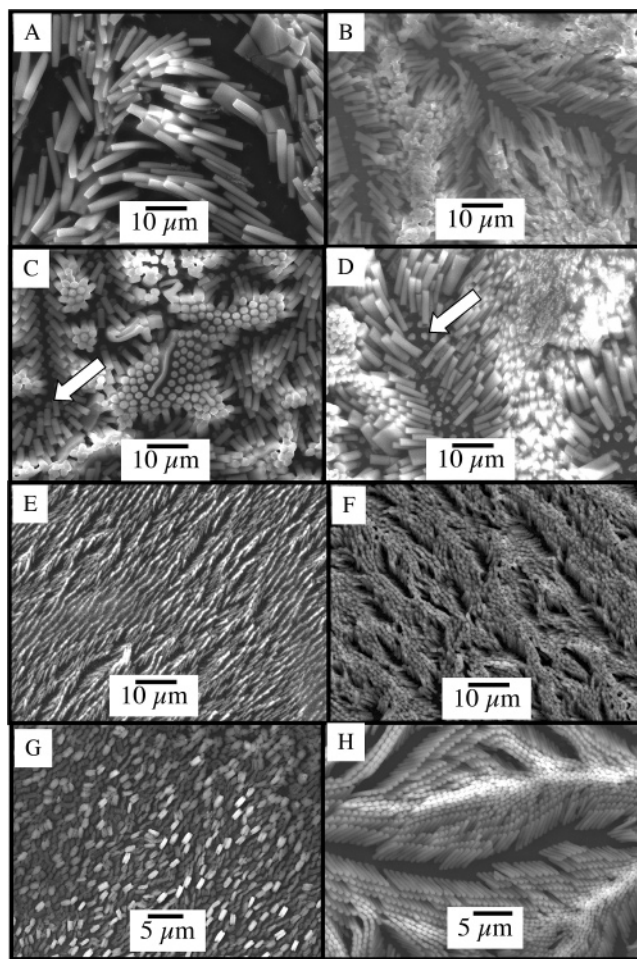


**Figure 3.** SEM images of the cylinder patterns obtained at various field intensities and concentrations. For A–D, the concentration of the solution is  $9.53 \times 10^{-3} \text{ mol L}^{-1}$ , the field intensity is 0.17 T for A, 0.33 T for B, 0.46 T for C, and 0.59 T for D. For E and F, the concentration is  $4.76 \times 10^{-4} \text{ mol L}^{-1}$  and the field intensities are 0.17 and 0.59 T, respectively. For G and H, the concentration is  $2.38 \times 10^{-4} \text{ mol L}^{-1}$  and the field intensities are 0.17 and 0.59 T, respectively.

structure. In a video study,<sup>10</sup> it has been observed that the cylinders are upright and collapse at the end of the evaporation process. This is due to capillary forces.

A more quantitative study is performed to describe the influence of the strength of the applied field during the deposition process at various nanocrystal concentrations. Let us consider three various nanocrystal concentrations submitted to various applied fields (0.17, 0.33, 0.46, and 0.59 T):

(i) At  $9.53 \times 10^{-3} \text{ mol L}^{-1}$ , the patterns shown in Figure 3A–D, obtained at various applied fields, show that the sizes (radius and height) of the mesostructures are not markedly influenced by the variation of the magnetic field.

(ii) At  $4.76 \times 10^{-4} \text{ mol L}^{-1}$ , the sizes of the cylinder patterns are reduced compared with those obtained at  $9.53 \times 10^{-3} \text{ mol L}^{-1}$ . Parts E and F of Figure 3 show only the two extreme fields (0.17 and 0.59 T, respectively). Similar behavior is observed for the various field strengths.

(iii) At  $2.38 \times 10^{-4} \text{ mol L}^{-1}$ , the pattern morphology is field strength independent. However, a further decrease in the size of the cylinders is observed (Figure 3G,H).

The radius ( $r_0$ ), the height ( $L$ ) of the cylinders, and the phase ratio  $\Phi$  characterize the mesoscopic pattern. The ratio of the magnetic phase to the total volume ( $\Phi$ ) is calculated from the cylinder radius and their separation ( $a$ ).

$$\Phi = \frac{\pi r_0^2}{(\sqrt{32})a^2} \quad (8)$$

These geometrical parameters are measured on the SEM image. The cylinder radius is obtained by measuring the cylinder diameter. It is rather easy to determine the cylinder length ( $L$ ) when the columns lie on the flat substrate. To determine  $\Phi$ , we need to measure the center-to-center distance ( $a$ ) between cylinders. This is not so easy because of the fact that the cylinders are collapsed. Thus, two methods are used: (i) We measure the distance between two bases of the cylinders when they can be observed in the SEM pictures (arrows in Figure 3C,D). (ii) The average surface area per cylinder is measured by counting the cylinders in a given large area on the substrate. From the average surface area  $s_h = (\sqrt{3}/2)a^2$ ,  $a$  can be calculated. We carefully check that these two methods give the same values within experimental error. The second method makes it possible to determine the space between two cylinders even when the bases of the cylinders are not visible. The characteristic sizes with their errors, that is, the radii ( $r_0$ ), the heights ( $L$ ), the separations ( $a$ ), and the phase ratios ( $\Phi$ ) of the structures, obtained at different magnetic fields and solution concentrations are reported in Table 1. The errors are calculated by taking into account the precision of the measurement (due to the magnification) and the size distribution of the cylinders. The experimental errors in  $\Phi$  are large because it depends on a quadratic function of both  $r_0$  and  $a$ . Note that, when the cylinders are too densely packed, the collapsing of the cylinders induces too much damage, or when the structures are not well-defined, as shown in Figure 3G,H, the required parameters cannot be measured. Table 1 contains the various parameters deduced from the SEM patterns obtained at various nanocrystal concentrations and various applied magnetic fields (samples 1, 2, 4, 7, 8, and 11 correspond to parts A–F of Figure 3, respectively). Samples 3–6 were obtained for the same field strength (0.46 T) and concentration ( $9.3 \times 10^{-3}$  mol L $^{-1}$ ). Also, for other conditions, several mesostructures were observed. However, they are not reported in Table 1 because all of the parameters necessary for the theory could not be determined. Please note that large differences in  $L$  and  $r_0$  appear for samples 3–6 that are made using the same concentration and magnetic field. This difference can be explained by the fact that the heights of the mesostructures cannot be controlled during the evaporation of the cobalt nanocrystal solution. Thus, different mesostructure heights are observed on the same substrate, which is the case for samples 3 and 4 or samples 5 and 6.

**3-2. Mechanism of the Mesostructure Formation.** The direct observation of the structure formation, during the evaporation process, can be followed by video microscopy.<sup>10</sup> However, the optical resolution is not high enough to determine its mechanism. Hexagonally ordered peaks of ferrofluid have actually been observed on macroscopic scales.<sup>24</sup> The formation of such patterns is explained by the normal-field Rosensweig instability,<sup>25</sup> which usually appears at the free surface of magnetic fluids subjected to a vertically oriented magnetic field. The peak formation is a specific case of the Rosensweig instability for a thin ferrofluid layer. In this case, the interface is between the atmosphere and the magnetic nanocrystal solution, and the interfacial tension is usually close to the solvent surface tension, which is 0.0184 N m $^{-1}$  for hexane.<sup>26</sup> According to Rosensweig, the presence of magnetic nanocrystals should not markedly modify this surface tension.<sup>25</sup> Another possible mechanism is based on the fact that, during the evaporation process, the increase in the nanocrystal concentration induces a liquid–gas phase transition. The one phase contains diluted nanocrystals, whereas the other is highly concentrated. The cylinders are formed before the end of the evaporation process by the latter phase. In this case, the interface is between two liquid phases, the nonmagnetic one and the magnetic one. The interfacial tension<sup>27</sup> in the demixed nanocrystal solution far from the critical point is expected to be about  $10^{-5}$  N m $^{-1}$ . In the theory developed above, the cylinder radius ( $r_0$ ) is a monotonically decreasing function of the interfacial tension. Table 2 lists the interfacial tensions, which are necessary to reproduce the same radii as those in the experiments (Table 1) for the applied fields, measured heights, and phase ratios. The calculated interfacial tension varies from  $2 \times 10^{-5}$  to  $10 \times 10^{-5}$  N m $^{-1}$ . These values are significantly too low for the first mechanism, whereas they are consistent with the second one. The variation of the interfacial surface tension between  $2 \times 10^{-5}$  and  $10 \times 10^{-5}$  N m $^{-1}$  can be explained by the accuracy of the experimental data. From experiments carried out with nanocrystals having an average diameter of 5.7 nm instead of 7.2 nm, similar surface tension values are deduced. On the basis of this finding, we conclude that the mesostructure formation is due to an aggregation of the cobalt nanocrystals yielding the magnetic phase (liquid–gas transition). These nanocrystal aggregates are surrounded by a highly diluted solution, the nonmagnetic phase. The observed phenomenon is caused by the labyrinthine instability and not by the Rosensweig instability, despite the presence of a free surface.

**3-3. Parameters Involved in the Control of the Mesostructure Size.** Let us now use an average  $\sigma$  value ( $5 \times 10^{-5}$

**TABLE 1: Values of the Radii ( $r_0$ ), Heights ( $L$ ), and Separations ( $a$ ) of the Cylinders for Mesostructures of Cobalt Nanocrystals Obtained at Various Field Strengths and Initial Concentrations of Cobalt<sup>a</sup>**

sample number	concentration [mol L $^{-1}$ ]	magnetic field [T]	$r_0$ [ $\mu$ m]	$L$ [ $\mu$ m]	$a$ ( $\mu$ m)	$\Phi$
1	$9.53 \times 10^{-3}$	$0.17 \pm 0.02$	$0.75 \pm 0.14$	$10 \pm 0.3$	$2.0 \pm 0.1$	$0.51 \pm 0.24$
2	$9.53 \times 10^{-3}$	$0.33 \pm 0.02$	$0.75 \pm 0.14$	$10 \pm 0.3$	$2.0 \pm 0.1$	$0.51 \pm 0.24$
3	$9.53 \times 10^{-3}$	$0.46 \pm 0.02$	$0.50 \pm 0.10$	$10 \pm 1$	$2.0 \pm 0.1$	$0.23 \pm 0.12$
4	$9.53 \times 10^{-3}$	$0.46 \pm 0.02$	$0.75 \pm 0.07$	$5.0 \pm 0.3$	$2.4 \pm 0.1$	$0.38 \pm 0.11$
5	$9.53 \times 10^{-3}$	$0.46 \pm 0.02$	$1.25 \pm 0.15$	$25 \pm 1$	$5.0 \pm 0.1$	$0.23 \pm 0.07$
6	$9.53 \times 10^{-3}$	$0.46 \pm 0.02$	$1.00 \pm 0.13$	$12 \pm 1$	$5.0 \pm 0.1$	$0.51 \pm 0.16$
7	$9.53 \times 10^{-3}$	$0.59 \pm 0.02$	$0.75 \pm 0.15$	$11 \pm 0.6$	$2.3 \pm 0.1$	$0.38 \pm 0.19$
8	$4.76 \times 10^{-4}$	$0.17 \pm 0.02$	$0.30 \pm 0.05$	$2.9 \pm 0.2$	$1.8 \pm 0.1$	$0.10 \pm 0.04$
9	$4.76 \times 10^{-4}$	$0.46 \pm 0.02$	$0.36 \pm 0.05$	$2.6 \pm 0.2$	$0.86 \pm 0.1$	$0.64 \pm 0.3$
10	$4.76 \times 10^{-4}$	$0.46 \pm 0.02$	$0.31 \pm 0.07$	$1.16 \pm 0.15$	$0.76 \pm 0.1$	$0.60 \pm 0.4$
11	$4.76 \times 10^{-4}$	$0.69 \pm 0.02$	$0.34 \pm 0.03$	$2.9 \pm 0.3$	$0.98 \pm 0.1$	$0.44 \pm 0.17$
12	$2.38 \times 10^{-4}$	$0.46 \pm 0.02$	$0.12 \pm 0.02$	$0.23 \pm 0.04$	$1.0 \pm 0.1$	$0.05 \pm 0.03$
13	$2.38 \times 10^{-4}$	$0.46 \pm 0.02$	$0.27 \pm 0.03$	$1.15 \pm 0.05$	$0.72 \pm 0.1$	$0.51 \pm 0.2$

<sup>a</sup> The phase ratios  $\Phi$  corresponding to these structures are also reported.

**TABLE 2: Surface Interfacial Tensions ( $\sigma$ ) Obtained by a Comparison of Theory with Experiments<sup>a</sup>**

sample number	magnetic field [T]	$L$ [ $\mu\text{m}$ ]	$\Phi$	$r_{0,\text{theory}}/L$	$r_{0,\text{exp}}/L$	$\sigma$ [ $\text{N m}^{-1}$ ]
1	$0.17 \pm 0.02$	$10 \pm 0.3$	$0.51 \pm 0.24$	$0.075 \pm 0.017$	0.116	$2.1 \times 10^{-5}$
2	$0.33 \pm 0.02$	$10 \pm 0.3$	$0.51 \pm 0.24$	$0.075 \pm 0.017$	0.110	$3.0 \times 10^{-5}$
3	$0.46 \pm 0.02$	$10 \pm 1$	$0.23 \pm 0.12$	$0.050 \pm 0.015$	0.057	$3.9 \times 10^{-5}$
4	$0.46 \pm 0.02$	$5.0 \pm 0.3$	$0.38 \pm 0.11$	$0.15 \pm 0.020$	0.105	$10.1 \times 10^{-5}$
5	$0.46 \pm 0.02$	$25 \pm 1$	$0.23 \pm 0.07$	$0.050 \pm 0.008$	0.035	$9.8 \times 10^{-5}$
6	$0.46 \pm 0.02$	$12 \pm 1$	$0.51 \pm 0.16$	$0.083 \pm 0.018$	0.084	$4.9 \times 10^{-5}$
7	$0.59 \pm 0.02$	$11 \pm 0.6$	$0.38 \pm 0.19$	$0.068 \pm 0.018$	0.068	$5.0 \times 10^{-5}$
8	$0.17 \pm 0.02$	$2.9 \pm 0.2$	$0.10 \pm 0.04$	$0.10 \pm 0.024$	0.11	$4.6 \times 10^{-5}$
9	$0.46 \pm 0.02$	$2.6 \pm 0.2$	$0.64 \pm 0.3$	$0.14 \pm 0.04$	0.24	$1.7 \times 10^{-5}$
10	$0.46 \pm 0.02$	$1.16 \pm 0.15$	$0.60 \pm 0.4$	$0.26 \pm 0.09$	0.33	$3.6 \times 10^{-5}$
11	$0.69 \pm 0.02$	$2.9 \pm 0.3$	$0.44 \pm 0.17$	$0.12 \pm 0.023$	0.15	$3.2 \times 10^{-5}$
12	$0.46 \pm 0.02$	$0.23 \pm 0.04$	$0.05 \pm 0.03$	$0.52 \pm 0.18$	0.33	$9.3 \times 10^{-5}$
13	$0.46 \pm 0.02$	$1.15 \pm 0.05$	$0.51 \pm 0.2$	$0.23 \pm 0.04$	0.28	$3.7 \times 10^{-5}$

<sup>a</sup> For the mesostructures presented in Table 1, the field strengths ( $B$ ), cylinder heights ( $L$ ), and reduced radii ( $r_{0,\text{exp}}/L$ ) are also reported. The theoretical reduced radius ( $r_{0,\text{theory}}/L$ ) is calculated using a surface tension of  $5 \times 10^{-5} \text{ N m}^{-1}$ .

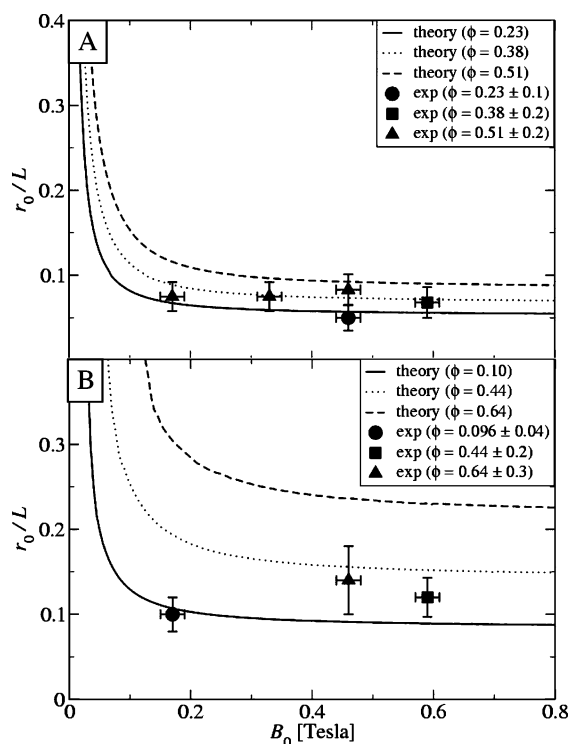


**Figure 4.** Dependence of the reduced cylinder radius  $r_0/L$  in hexagonal patterns on the external field. The theoretical curves for three different phase ratios  $\Phi$  are compared to the experimental data points. The results at heights of 10 and 2.8  $\mu\text{m}$  are shown in parts A and B, respectively.

$\text{N m}^{-1}$ ) to investigate the parameters, which control the sizes of the experimentally observed structures. We first recalculate reduced cylinder radii ( $r_0^* = r_0/L$ ) using the experimental conditions ( $H_0$ ,  $\Phi$ ,  $L$ ). Considering the experimental error, the calculated values  $r_{0,\text{theory}}^*$  behave similarly to the experimental  $r_{0,\text{exp}}^*$  ones (see Table 2). It is worth noting that the theoretical free energies were determined for every mesostructure in Table 2. However, because these values depend on the height and the phase ratio, a direct comparison of the free energies obtained for different  $L$  and  $\Phi$  values is not suitable. Therefore, these values of free energy are not reported in Table 2.

**3-3-1. Influence of the Applied Magnetic Field.** We benefit from the fact that several experimental mesostructures obtained at different field intensities have similar cylinder heights. For the comparison of these structures, the influence of the height can be neglected. This is the case for samples 1–3, 6, and 7 in Table 1, which have heights of around 10  $\mu\text{m}$ , and also samples

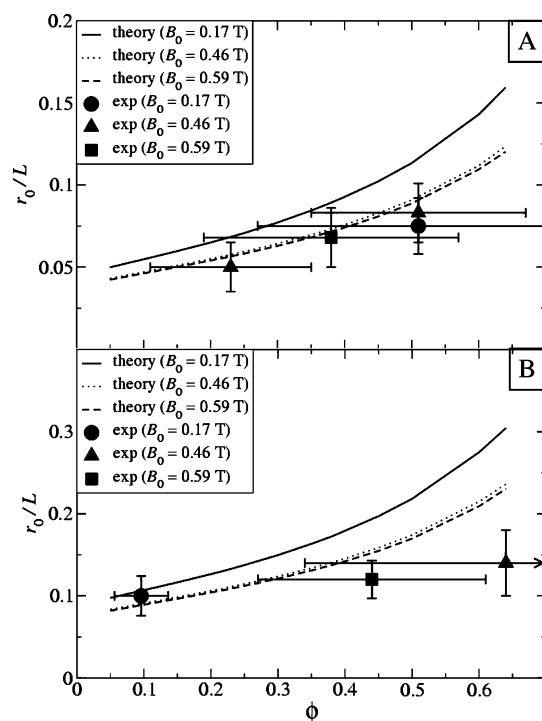


**Figure 5.** Dependence of the reduced cylinder radius  $r_0/L$  in hexagonal patterns on the phase ratio. The theoretical curves for three different field strengths ( $H_0$ ) are compared to the experimental data points. The results at heights of 10 and 2.8  $\mu\text{m}$  are shown in parts A and B, respectively.

8, 9, and 11 have similar heights (about 2.8  $\mu\text{m}$ ). In Figure 4A,B, the theoretical reduced radii  $r_0/L$  are plotted using heights of 10 and 2.8  $\mu\text{m}$ , respectively. The three curves in each figure correspond to the phase ratios observed for the experimental data points. The theoretical curves show that the experiments have been carried out at field intensities where the pattern size slightly varies with the field. This is due to a saturation effect caused by the nonlinearity of the magnetization curve (Figure 1). To understand the trend observed for the experimental data points in Figure 4A,B, the variation of  $r_0/L$  with  $\Phi$  as predicted by the theory must be considered. For example, in Figure 4A, the sphere and the square can be compared to the triangles by taking into account the theoretically predicted increase of  $r_0/L$  with  $\Phi$ . The experimental data are in agreement with the theoretical curves, especially considering the error in the phase ratio. For example, in Figure 4A, the experimental point at a field of 0.17 T and a  $\Phi$  of 0.51 does not seem to fit on the



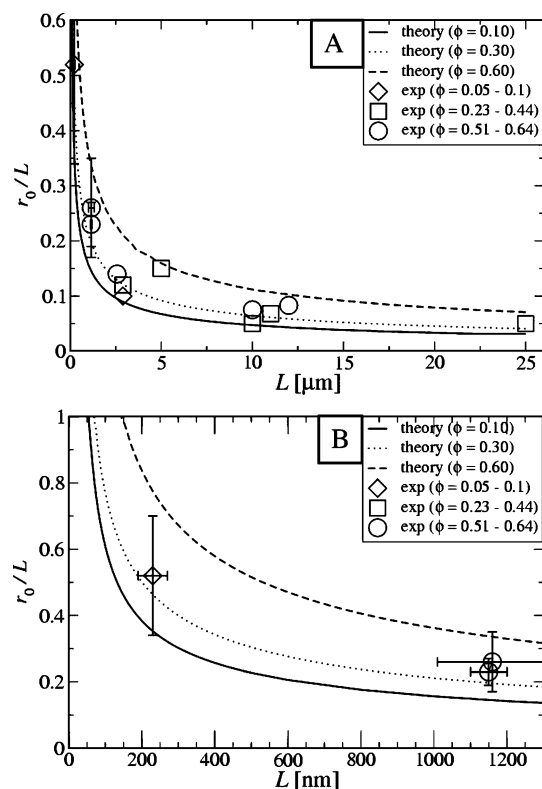


**Figure 6.** Comparison of the experimental and theoretical variations of the reduced radius as a function of the cylinder height. The theoretical results for three different phase ratios are shown. B is a magnification of A, to show the evolution of the reduced radius at small heights.

theoretical curve. However, the deviation can be explained by the error in  $\Phi$ . We conclude that the invariance of the mesostructures with the strength of the applied magnetic field is due to the fact that, in this range, the magnetic response remains unchanged (nonlinear regime). Note that, in a former paper,<sup>12</sup> we have shown that older experimental data obtained using Hele-Shaw cells present no field saturation.

**3-3-2. Influence of the Phase Ratio.** To neglect the influence of the pattern height, the same two sets of experimental data points as those employed above for the study of the field dependence are used. The phase ratio is directly related to the separation  $a_0$  between cylinder centers. Thus, for the same cylinder radius and height, an increase in the phase ratio is related to a decrease in the distance  $a_0$ , according to eq 1. Therefore, the study of the influence of  $\Phi$  on  $r_0$  gives information on the impact of the surrounding cylinders on the radius of one cylinder. Parts A and B of Figure 5 show the variation of the reduced radius with  $\Phi$  for heights of 10 and 2.8  $\mu\text{m}$ , respectively. In both figures, the curves for the three magnetic field intensities corresponding to the experimental data are plotted. Theory predicts, for both heights, an increase in the reduced radius with phase ratio. The experimental data points show the same behavior in both figures. However, in particular for that in Figure 5B, the experimental increase is smaller than the theoretical prediction. Nevertheless, because of the significant error in the experimentally measured phase ratio, the comparison between theory and experiments is limited. This experimentally and theoretically observed increase in the reduced radius with  $\Phi$  can be explained as follows. The observed mesostructures appear because of a competition of interfacial and magnetic energy.<sup>19</sup> An increase in  $\Phi$  leads to a lower demagnetization field. When the demagnetization field

decreases, the magnetic energy term becomes smaller. This favors larger reduced radii, as experimentally observed.

**3-3-3. Influence of the Height.** Figure 6 shows the theoretical evolution of  $r_0/L$  as a function of  $L$  for three representative  $\Phi$  values. For cylinder heights above 5  $\mu\text{m}$ , the cylinder reduced radius varies only slightly with  $L$ . For smaller pattern heights, the reduced radius drastically increases on decreasing  $L$ . For comparison, the experimental data points taken from Table 2 are plotted in Figure 6. For large pattern heights, the size of the symbols indicates the experimental error. At smaller pattern heights, the experimental error bars are explicitly shown because they are significantly larger than the symbol size. Obviously, the experiments and the theory are in good agreement. In particular, the reduced radius of 0.5 observed at a height of 0.23  $\mu\text{m}$  (sample 12) is in excellent agreement with the theoretical prediction (Figure 6A). The growth of  $r_0/L$  can be explained by the linear dependence of the magnetic energy on the pattern height. We can conclude that the pattern height is a key factor, which controls the size of patterns at submicrometric scales.

#### 4. Conclusion

Cylindrical mesostructures of cobalt nanocrystals are obtained by a slow evaporation of these particles dispersed in hexane and subjected to an applied magnetic field perpendicular to the substrate. Most of the cylinders are collapsed; however, in some cases, upright cylinders remaining in hexagonal arrays are observed. No influence of the magnetic field intensities on the morphology of the mesostructure is experimentally noted. When the concentration of the nanocrystal solution is lowered, the sizes (radius and height) of the columns are decreased. A theoretical model based on the minimization of the total free energy is developed. Within this theory, the cylinder radius is a function of the field, the phase ratio, and the cylinder height. Good general agreement between experiment and theory is found. From a comparison of theoretical values with experimental data, an average interfacial surface tension of  $5 \times 10^{-5} \text{ N m}^{-1}$  is calculated. It is deduced that the formation of the mesostructures is due to labyrinthine instabilities. To the best of our knowledge, this is the first time that this type of instability has been observed for a system with a free surface. From experimental data and the theoretical model, it is concluded that the phase ratio and the height govern the pattern geometry. However, no influence of the magnetic field intensities is noted, and this is explained in terms of no changes in the magnetic response in the used intensity range. Our method of preparation of cobalt nanocrystal patterns can be employed for the fabrication of artificial mesostructures of several hundreds of nanometers.

#### References and Notes

- (1) Legrand, J.; Ngo, A. T.; Petit, C.; Pileni, M. P. *Adv. Mater. (Weinheim, Ger.)* **2001**, *13*, 58.
- (2) Cebers, A.; Maiorov, M. M. *Magnetohydrodynamics (NY)* **1980**, *16*, 21.
- (3) Rosensweig, R. E.; Zahn, M.; Shumovich, R. J. *Magn. Magn. Mater.* **1983**, *39*, 127.
- (4) Bacri, J.-C.; Perzynski, R.; Salin, D. *Endeavour* **1988**, *12*, 76.
- (5) Elias, F.; Flament, C.; Bacri, J.-C.; Neveu, S. *J. Phys. I* **1997**, *7*, 711.
- (6) Hong, C. Y.; Jang, I. J.; Horng, H. E.; Hsu, C. J.; Yao, Y. D.; Yang, H. C. *J. Appl. Phys.* **1997**, *81*, 4275.
- (7) Dickstein, A. J.; Erramilli, S.; Goldstein, R. E.; Jackson, D. P.; Langer, S. A. *Science* **1993**, *261*, 1012.
- (8) Ytreberg, F. M.; McKay, S. R. *Phys. Rev. E: Stat. Phys., Plasmas, Fluids, Relat. Interdiscip. Top.* **2000**, *E61*, 4107.
- (9) Richardi, J.; Ingert, D.; Pileni, M. P. *J. Phys. Chem. B* **2002**, *106*, 1521.
- (10) Germain, V. Unpublished data.

- (11) Whitesides, G. M.; Grzybowski, B. *Science* **2002**, 295, 2418.
- (12) Richardi, J.; Pileni, M. P. *Phys. Rev. E: Stat. Phys., Plasmas, Fluids, Relat. Interdiscip. Top.* **2004**, 69, 16304.
- (13) Lisiecki, I.; Pileni, M. P. *Langmuir* **2003**, 19, 9486.
- (14) Petit, C.; Lixon, P.; Pileni, M. P. *J. Phys. Chem.* **1990**, 94, 1598.
- (15) The scanning electron microscope used is a JEOL 5510 LV.
- (16) Flamant, C.; Laci, S.; Bacri, J. C.; Cebers, A.; Neveu, S.; Perzynski, R. *Phys. Rev. E: Stat. Phys., Plasmas, Fluids, Relat. Interdiscip. Top.* **1996**, 53, 4801.
- (17) Lacoste, D.; Lubensky, T. C. *Phys. Rev. E: Stat. Phys., Plasmas, Fluids, Relat. Interdiscip. Top.* **2001**, 64, 041506.
- (18) Lisiecki, I.; Albouy, P. A.; Pileni, M. P. *Adv. Mater. (Weinheim, Ger.)* **2003**, 15, 712.
- (19) Richardi, J.; Ingert, D.; Pileni, M. P. *Phys. Rev. E: Stat. Phys., Plasmas, Fluids, Relat. Interdiscip. Top.* **2002**, 66, 046306.
- (20) Richardi, J.; Pileni, M. P. *Eur. Phys. J. E* **2004**, 13, 99.
- (21) The Fortran package HEXALAB is a highly optimized code of about 10 thousand statements, which calculates the geometry and energy of magnetic fluid patterns. The kinds of patterns are not restricted to hexagonal or labyrinthine ones. HEXALAB was developed by J. Richardi at the LM2N (direction: M. P. Pileni).
- (22) Hong, C. Y.; Horng, H. E.; Kuo, F. C.; Yang, S. Y.; Yang, H. C.; Wu, J. M. *Appl. Phys. Lett.* **1999**, 75 (15), 2196.
- (23) Leo, G.; Chushkin, Y.; Luby, S.; Majkova, E.; Kostic, I.; Ulmeanu, M.; Luches, A.; Giersig, M.; Hilgendorff, M. *Mater. Sci. Eng., C* **2003**, 23, 949.
- (24) Zahn, M. *J. Nanopart. Res.* **2001**, 3, 73.
- (25) Cowley, M. D.; Rosensweig, R. E. *J. Fluid Mech.* **1967**, 30, 671.
- (26) Hunter, R. J. *Foundations of Colloid Science*; Oxford University Press: Oxford, U.K., 2001.
- (27) de Hoog, E. H. A.; Lekkerkerker, H. N. W. *J. Phys. Chem. B* **1999**, 103, 5274.